

www.acsaem.org Article

Two-Dimensional MXenes Mo₂Ti₂C₃T_z and Mo₂TiC₂T_z: Microscopic Conductivity and Dynamics of Photoexcited Carriers

Guangjiang Li, Varun Natu, Teng Shi, Michel W. Barsoum, and Lyubov V. Titova*



Cite This: ACS Appl. Energy Mater. 2020, 3, 1530–1539



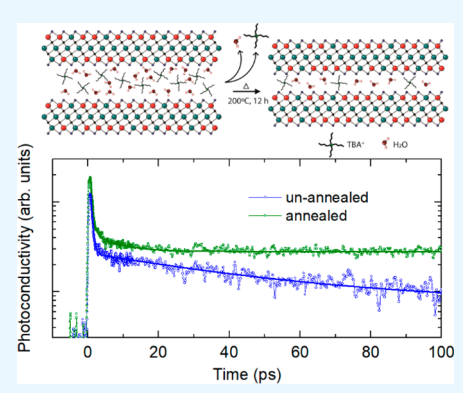
ACCESS

Metrics & More

Article Recommendations

Supporting Information

ABSTRACT: MXenes are a recently discovered family of two-dimensional transition metal carbides, nitrides, and carbonitrides with electronic properties that can be tuned by their chemistry and structure. Herein THz spectroscopy was used to investigate the microscopic conductivity and photoexcited charge carrier dynamics in two Mo-based MXenes: $Mo_2Ti_2C_3T_z$ and $Mo_2TiC_2T_z$. We find that both have high intrinsic carrier densities ($\sim 10^{20}$ cm⁻³ in $Mo_2Ti_2C_3T_z$ and $\sim 10^{19}$ cm⁻³ in $Mo_2TiC_2T_z$) and mobilities and exhibit high conductivities within individual nanosheets. Optical excitations result in a transient conductivity increase in both compositions, in stark contrast with the most studied member of the MXene family, $Ti_3C_2T_z$, where photoexcitation suppresses the conductivity for nanoseconds. Deintercalation of water, and other species, from between the nanosheets by mild vacuum annealing at 200 °C further improves the long-range, internanosheet transport of the photoexcited carriers and increases their lifetime. High, and long-lived, photoinduced conductivity that can be engineered by substituting Mo for Ti renders these Mo-based MXenes attractive for a variety of optoelectronic, sensing, and photoelectrochemical applications.



KEYWORDS: MXenes, microscopic conductivity, photoexcited charge carrier dynamics, THz spectroscopy

1. INTRODUCTION

MXenes are an emergent family of 2D transition metal carbides, nitrides, and carbonitrides with the general formula $M_{n+1}X_nT_z$, where M is an early transition metal, X is carbon and/or a nitrogen, and n is 1, 2, or 3. T_z stands for surface terminations, e.g., -OH, -F, =O. Their electronic properties have been predicted to span the range from highly conductive metallic to semimetallic, semiconducting, and even topologically insulating. $^{1-7}$

Some MXenes exhibit phenomena such as record high volumetric capacitances and optical nonlinearity, suggesting that they can find use in charge storage, transparent flexible conductors, electromagnetic shielding, and nonlinear optical devices. This wide variety of properties and potential applications underscores the need to understand the mechanisms of carrier transport in these new materials as a function of their chemical composition, terminations, and processing method.

To fabricate MXenes, the A element such as Al is removed from a parent MAX phase, typically by etching, mostly in F-containing aqueous media. During the etching process, the A layers are replaced by the surface terminations, T_z. Once a, typically aqueous, colloidal suspension of MXene is formed, films can be readily formed from the latter by coating them on substrates or filteration. In these films, water molecules and cations occupy the space between individual MXene nanosheets and can affect transport properties, such that removing

them by annealing can sometimes lead to dramatic changes in transport properties. The transport properties of MXene films result from a complicated interplay of intrananosheet carrier transport determined mainly by the properties of the $M_{n+1}X_n$ cores and affected by their point and other defects and long-range, internanosheets transport. The latter carrier motion is sensitive not only to the nature of T_z but also to the properties of the nanosheet edges and any species intercalated between the them.

The titanium carbide MXene ${\rm Ti_3C_2T_z}$ was the first discovered and has since been the most extensively studied. Studies have demonstrated that not only are individual ${\rm Ti_3C_2T_z}$ MXene flakes metallic with a high carrier density and mobility, consistent with DFT calculations that predict high density of states at the Fermi level ${\rm E_F}$, but macroscopic ${\rm Ti_3C_2T_z}$ films retain metallic-like conductivity with positive ${\rm dR/dT}$ over a broad temperature range. The metallicity is also evidenced by single nanosheet measurements. 18

The situation is more complicated in molybdenum, Mobased MXenes. While nonspin-polarized DFT calculations predict them to be metallic with significant DOS at the $E_{\rm F}$, ¹⁹

Received: October 5, 2019 Accepted: January 13, 2020 Published: January 13, 2020



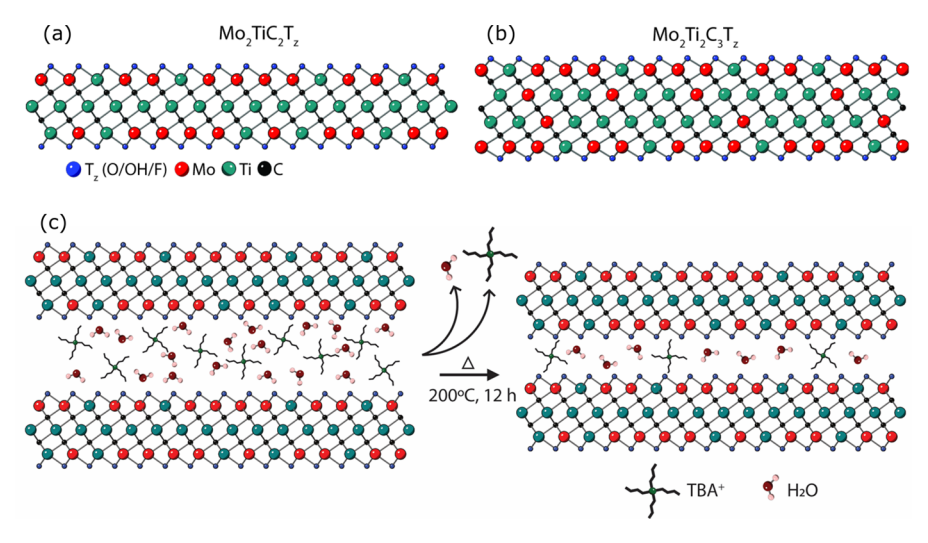


Figure 1. Schematic of (a) $Mo_2TiC_2T_z$ and (b) $Mo_2Ti_2C_3T_z$ structures. (c) Effect of vacuum annealing on a film structure and internanosheet distance.

accounting for spin polarization opens a small (tens of meV) gap in OH and -F terminated Mo-MXenes but not in O-terminated Mo-MXenes.³

Experiments have shown that replacing some or all of the Ti with Mo in a MXene structure results in a lower carrier density, and a semiconductor-like behavior has been reported in several studies of multilayer Mo-MXene films as resistivity showed a slow increase at lower temperatures (dR/dT < 0). 1,3,7,19 However, systematic temperature-dependent magneto-transport measurements of Mo-based MXenes revealed that they behave like disordered systems, not unlike granular metals. Their long-range conductivity is limited by the internanosheet carrier transfer which occurs mainly by variable range hopping (VRH), with a contribution from a thermally activated mechanism at higher temperatures. These experiments also demonstrated that conductivity is strongly dependent on the internanosheet distance and increases by orders of magnitude when annealing reduces this distance by releasing the water and other intercalants from the interflake space. Finally, vacuum annealing of Mo₂TiC₂T₂ at temperatures (up to 775 °C) that are sufficiently high to eliminate most intercalated species was found to reverse the sign of dR/dT from negative to positive, establishing the intrananosheet metallicity of $Mo_2TiC_2T_{zt}$ and demonstrating that the dR/dT< 0 behavior of multilayer Mo-MXenes is most probably caused by the internanosheet species.⁷ However, an exact picture of the microscopic conductivity and charge carrier dynamics in Mo-MXenes remains incomplete.

Terahertz (THz) spectroscopy, an all-optical, noncontact probe of microscopic conductivity and equilibrium and nonequilibrium free carrier dynamics, can provide just the insight needed for to obtain a comprehensive picture of the transport properties over microscopic length scales. With a THz pulse bandwidth of 0.25-2.1 THz (or, equivalently, 1-10 meV in terms of photon energy), free carrier absorption results in attenuation of the THz probe pulse transmitted through a MXene film. The strength of this absorption is governed by the free carrier density and mobility. THz spectroscopy yields a frequency-resolved complex conductivity without the complication of electrical contacts. It is sensitive to the carrier motion on length scales, L, of tens to hundreds of nanometers, determined by the probing THz frequency ω according to

 $L(\omega) \propto (D/\omega)^{1/2}$, where D is the diffusion constant. ^{22,23} THz conductivity spectra thus represent microscopic carrier transport, averaged over many nanosheets present in approximately a 1–2 mm diameter THz probe spot size. ²⁴ Lastly, timeresolved THz spectroscopy (TRTS) takes advantage of the short duration of THz pulses to examine the effects of photoexcitation on conductivity and carrier dynamics with subpicosecond, ps, time resolution. ^{20,25–29} In metals, changes in conductivity in response to optical excitation include contributions of both intraband free carrier absorption and interband transitions which can introduce additional free carriers if the excitation energy is higher than the interband transition threshold. ³⁰

Recently, we reported on the THz spectroscopic study of a metallic $\mathrm{Ti}_3\mathrm{C}_2\mathrm{T}_z$ MXene film. We found that it has a high, $\sim 2 \times 10^{21}$ cm⁻³, intrinsic charge carrier density, relatively high (~ 34 cm²/(V s)) mobility of carriers *within* individual $\mathrm{Ti}_3\mathrm{C}_2\mathrm{T}_z$ nanosheets, and a long-range mobility of ~ 1 cm²/(V s), limited by internanosheet transport. In this metallic MXene, photoexcitation with 100 fs duration, 800 nm laser pulses induces transient suppression of conductivity, which recovers over hundreds of picoseconds. This transient suppression is believed to be due to the excitation-induced reduction in mobility of existing free carriers playing a more important role than a small increase in carrier density by interband excitation.

Here, we exploit the ability of THz spectroscopy to glean information about both internanosheet and intrananosheet contributions to conductivity to investigate the microscopic conductivity and carrier dynamics in two Mo-based MXenes, $\text{Mo}_2\text{Ti}_2\text{C}_3\text{T}_z$ and $\text{Mo}_2\text{Ti}\text{C}_2\text{T}_z$ (Figure 1a,b) films. Earlier transport measurements demonstrated that intercalation of water and tetrabutylammonium cations (TBA+) between the nanosheets that occurs during film preparation increases the internanosheet spacings and electrical resistances, resulting in negative dR/dT values. Vacuum annealing has been found to increase conductivity and reduce the internanosheet distances by releasing some of the intercalants (Figure 1c). In this study, we investigated how a mild (200 °C) vacuum anneal impacts transport properties of these two Mo-based MXenes.

One finding of this work is the dramatically different response of the Mo-based MXenes to photoexcitation compared to that of ${\rm Ti}_3{\rm C}_2{\rm T}_z$. Unlike ${\rm Ti}_3{\rm C}_2{\rm T}_z$ where optical

excitation suppresses conductivity, here there is a long-lived increase in photoconductivity in both $Mo_2Ti_2C_3T_z$ and $Mo_2TiC_2T_z$, with a lifetime that can be increased by annealing. We hypothesize that over an order of magnitude lower intrinsic carrier density ($\sim\!10^{20}~\rm cm^{-3}$ vs $\sim\!10^{21}~\rm cm^{-3}$ in $Ti_3C_2T_z)$ makes the interband carrier excitation the most pronounced effect of photoexcitation on conductivity in Mo-based MXenes. These findings highlight the broad range of optoelectronic properties of metallic MXenes, where substituting Ti for Mo at some of the transition metal sites and changing the interlayer spacing by annealing can also be used to engineer the transient photoconductive response.

2. EXPERIMENTAL DETAILS

2a. Samples. The MAXpowders were made by mixing molybdenum, Mo (-325 mesh, Alfa Aesar), titanium, Ti (-325 mesh, Alfa Aesar), aluminum, Al (-325 mesh, Alfa Aesar), and graphite, C (-300 mesh, Alfa Aesar), powders in molar ratios (Mo:Ti:Al:C) of 2:1:1.1:2 and 2:2:1.1:2.8 for Mo₂TiAlC₂ and Mo₂Ti₂AlC₃, respectively. The mixed powders were ball milled using zirconia balls in plastic containers for 24 h at 70 rpm and then heated under flowing argon (Ar) at 1600 °C for 4 h. The heating and cooling rates were set at 5 °C/min. The resulting loosely sintered blocks were ground using a milling bit on a drill press and the resulting powders passed through a 400 mesh (particle size $< 38 \mu m$) sieve to use for further experiments.¹⁹ To etch the resulting MAX phases, 1 g of sieved MAX powders was slowly added to 10 mL of 50% HF solution and stirred for 72 h at 55 °C and 500 rpm. The resulting slurry was transferred into a 50 mL centrifuge tube, and DI water was added to completely fill the remaining volume. It was then centrifuged at 3500 rpm for 60 s, and the resulting clear supernatant was discarded after which the washing was repeated until the pH of the solution was ≈ 7 .

To aid in the dispersion of the nanosheets, 1 mL of 1.5 M tetrabutylammonium hydroxide, TBAOH, solution is added to the resulting sediment. The mixture was then shaken using a vortex shaker for 0.5 h. Then 200 proof ethanol, EtOH, was added to fill the remaining volume of the centrifuge tube, shaken for 120 s, and centrifuged at 3500 rpm for 60 s. The clear EtOH supernatant was then discarded, and the process was repeated two more times. EtOH is used because it prevents the MXene nanosheets from deflocculating and washes away any excess TBAOH. After the last wash, the EtOH was discarded, and 30 mL of deionized, DI, water was added to the MXene slurry which was then hand shaken for 0.5 h to form a MXene colloidal suspension. To separate the nondelaminated multilayer MXene and unetched MAX phase particles, the colloid is centrifuged at 3500 rpm for 0.5 h, and the supernatant is stored for further use.

For the THz measurements, an ~80 nm thick film of Mo₂Ti₂C₃T_z was spin-coated onto 1 mm thick quartz substrates (Figure S1). XRD patterns of this film showed that the d spacing between nanosheets was 3.2 nm. Since we could not produce a high enough colloid concentration for the Mo₂TiC₂T_z composition for spin coating, in this case a film was produced by drop-casting the colloidal suspension directly onto a quartz substrate to yield a thicker (~1300 nm, Figure S1) film that XRD indicated contained some unreacted Ti₃AlC₂ (see Figure S3). The optical absorption coefficient (Figure S2) for this composition is lower than that for Mo₂Ti₂C₃T_z. Samples were cut in half, and one part of each sample was annealed for 12 h in vacuum (<20 mTorr) at 200 °C. To understand the effect annealing on the films, XRD patterns were obtained after annealing and compared to those before annealing. Figure S3 shows that upon annealing the d spacing of the Mo₂Ti₂C₃T_z sample decreased from 3.2 to 2.0 nm. The results for the Mo₂TiC₂T_z films were more ambiguous.

2b. THz Spectroscopy. THz spectroscopy measurements were carried out as described previously and are illustrated schematically in Figure 2. 15,26,27 In brief, picosecond-long THz pulses with the bandwidth between 0.25 and 2.1 THz (1–9 meV) are generated by optical rectification of 100 fs, 800 nm pulses in a 1 mm thick [110]

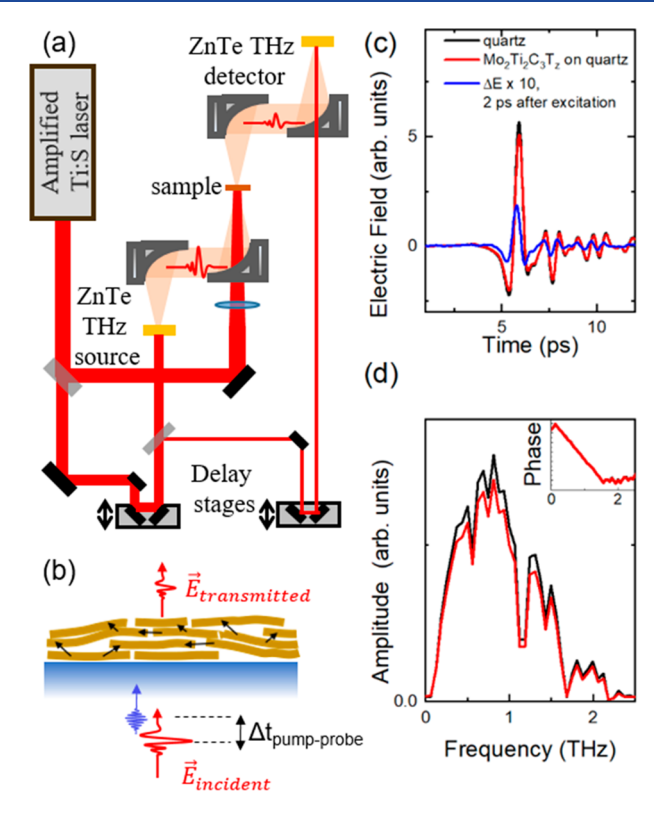


Figure 2. (a) Schematic diagram of THz TDS and TRTS. (b) Probing motion of photoexcited carriers in the MXene nanosheet by THz probe pulses. (c) THz waveforms transmitted through the substrate, through an MXene film on a quartz substrate, and the photoinduced change in the transmitted waveform 2 ps after excitation with a ~256 μ J/cm², 800 nm pulse. Comparing, in the frequency domain, the magnitude and phase (d) of THz pulses transmitted through the substrate with and without an MXene film yields a complex conductivity $\hat{\sigma}(\omega) = \sigma_1 + i\omega_2$.

ZnTe crystal. The pulses were focused onto the sample using off-axis parabolic mirrors (Figure 2a). At normal incidence, the THz pulses probe conductivity parallel to the substrate and, therefore, mainly in the basal plane of the nanosheets comprising the MXene films (Figure 2b), which is of particular interest as transport in MXenes is predominantly two-dimensional.³¹ Transmitted THz pulses are detected using free-space electro-optic sampling in a second 1 mm thick [110] ZnTe crystal.

In THz TDS, coherent detection of the amplitude and phase of THz probe pulses (Figure 2c) in the time domain allows for the extraction of a sample's frequency-dependent complex conductivity by comparing, in the frequency domain, the amplitudes and phases of the THz pulses transmitted through the substrate alone and the sample on the substrate (Figure 2d). All experiments were carried out under ambient conditions, with humidity in the 30–60% range. The series of dips in the THz amplitude spectrum (Figure 2d) represents absorption by atmospheric water vapor. To account for frequency-dependent variation of THz probe amplitude, all fits of the THz spectra discussed below were weighted by the corresponding THz amplitude spectrum.

To investigate the effects of optical excitation on the conductivity of our films, we used 800 nm (or 1.55 eV), 100 fs pulses as the optical pump and detected the photoinduced changes in the complex THz conductivity using a time-delayed THz probe pulse. As the low energy THz pulses are absorbed by the free, mobile carriers in the films, we probe the impact of the photoexcitation on the conductivity by following the optical pump-induced changes in the THz absorption as a function of the optical pump—THz probe delay. In fact, in the limit of small photoinduced changes, the negative change in the transmission of the THz probe pulse peak is proportional to the

transient change in the conductivity, or the photoconductivity, since $-\Delta T(t)/T \propto \Delta \sigma(t)$.

3. RESULTS AND DISCUSSION

3a. THz TDS: Intrinsic Microscopic Conductivity. Complex, frequency-resolved THz conductivity for MXenes both before and after a mild, 200 °C, anneal in vacuum are shown in Figure 3. First, comparison of the magnitude of the

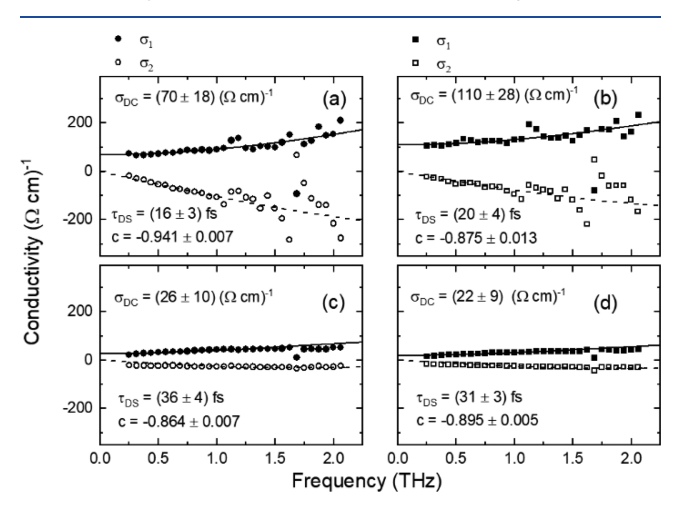


Figure 3. TDS of Mo₂Ti₂C₃T_z, (a) as deposited and (b) after a mild 200 °C vacuum annealing. (c) Same as (a) but for Mo₂TiC₂T_z, and (d) same as (b) but for Mo₂TiC₂T_z. Solid symbols represent real and open symbols represent imaginary conductivity, with lines showing global fits of both the real and imaginary conductivity to the Drude–Smith model with parameters $\sigma_{\rm DC}$, $\tau_{\rm DS}$, and c indicated on individual panels.

real conductivity (σ_1 , solid symbols) reveals that increase in the fraction of Mo correlates with increased conductivity i, an observation that is consistent with DC electronic measurements. ^{1,31} Analysis of the spectral shape of complex frequency-resolved conductivity yields additional information about the microscopic conductivity and contributions of intrananosheet and internanosheet transport.

We model the complex conductivity with a phenomenological Drude–Smith model, a modification of the free carrier Drude conductivity that accounts for localization of the mobile carriers on length scales commensurate with their mean free path, such as localization within individual nanosheets. ^{27,33–41} Complex frequency-resolved conductivity is given as $\tilde{\sigma}(\omega) = \frac{\sigma_0}{1-i\omega\tau_{DS}}(1+\frac{c}{1-i\omega\tau_{DS}}) \text{ where } \tau_{DC} \text{ is a carrier relaxation}$ time, $\sigma_0 = \frac{Ne^2\tau_{DS}}{m^2}, \ N \text{ is the intrinsic charge carrier density}$

time, $\sigma_0 = \frac{Nc \ t_{DS}}{m^*}$, N is the intrinsic charge carrier density and m^* is the carrier effective mass. In this formalism, the DC conductivity is given by $\sigma_{DC} = \sigma_0(1+c)$, where c is a phenomenological parameter that is a measure of carrier localization over the probed length scales. When c=0, the system is fully percolated and carriers move throughout the sample unimpeded. For c=-1, the σ_{DC} is suppressed as the carriers are localized over short distances. In the case of MXene films, tested herein, the c-parameter can be interpreted as a measure of internanosheet transport, and the long-range conductivity in the DC limit is expressed by the equation given above.

Short-range carrier mobility within the nanosheets can be calculated as $\mu_{short-range} = \frac{e\tau_{DS}}{m^*}$ if m^* is known, and the long-

range mobility is then given as $\mu_{long-range} = \mu_{short-range}(1 + c)$. The lines in Figure 3 represent global fits of both the real and the imaginary conductivity components to the Drude-Smith model with fitting parameters $\sigma_{\rm DC}$, $au_{\rm DC}$, and c indicated on the individual panels. The intrinsic THz conductivity measured by the TDS shows that both Mo₂Ti₂C₃T_z and Mo₂TiC₂T_z have considerable densities of free, delocalized carriers that attenuate the THz probe pulses via free carrier absorption. As the carrier effective mass in these MXenes is yet to be determined, we assume here that $m^* = m_e$, for the purposes of comparing intrinsic carrier densities and mobilities and elucidating the effects of annealing on those parameters. This approximation also assumes that the carrier effective mass is equal in both compositions. With these assumptions, we estimate the intrinsic carrier densities to be $\sim 2.5 \times 10^{20} \text{ cm}^{-3}$ for $Mo_2Ti_2C_3T_z$ and $\sim 0.2 \times 10^{20}$ cm⁻³ for $Mo_2TiC_2T_z$. While these values are over an order of magnitude lower compared to those of Ti₃C₂T_z films, ^{15,18} they are still significantly high, consistent with the metallic nature of these MXenes. 1,7

Given that the c-parameter is close to -1 and the real conductivity component decreases at lower frequencies, it is reasonable to conclude that the materials' nanosheet edges have a detrimental effect on the long-range conductivity. Such suppression of the real conductivity at lower frequencies is a hallmark of a system where grain boundaries or potential fluctuations impede long-range carrier transport and is observed in many granular and nanostructured materials. $^{33,34,41-43}$

Again assuming $m^* \approx m_e$, we estimate that the intrinsic, intrananosheet mobility in $Mo_2Ti_2C_3T_z$ is $\mu_{short-range} \sim 30$ cm²/ (V s), while the long-range, internanosheet mobility is ∼17 times lower. Likewise, for $Mo_2TiC_2T_z$, $\mu_{short-range} \sim 60 \text{ cm}^2/(\text{V})$ s), and the long-range mobility is ~8 times lower. This observation of the internanosheet transport being strongly impeded agrees well with our previous conclusion, viz., VRH and thermally activated hopping internanosheet transport being rate-limiting, reached from analysis of temperaturedependent conventional DC conductivity measurements. We also find that, despite a shorter relaxation time and a stronger suppression of internanosheet conductivity, Mo₂Ti₂C₃T₂ is more conductive compared to Mo₂TiC₂T_z, owing to a higher free carrier density. Along the same lines DFT calculations on $Mo_2Ti_2C_2O_2$ and $Mo_2TiC_2O_2$ indicate that the DOS at E_F in the latter is ≈ 3 times lower than the former consistent with the conclusions reached herein. We note in passing that DFT predicts that only O-terminated Mo-based MXenes are metallic. Others are predicted to have small band gaps, for which little evidence is found herein or elsewhere.

Intriguingly, at $\sim 30~{\rm cm^2/(V~s)}$, the intrinsic conductivity of ${\rm Mo_2Ti_2C_3T_z}$ is half that of ${\rm Mo_2TiC_2T_z}$. To explain this observation we refer to a recent XPS study of the Mo-based MXenes explored here, ⁴⁴ where we concluded that (i) the Ti atoms that substitute for Mo in the outer layers are dissolved during the etching procedure and (ii) the fraction of Ti in the Mo layers is higher in ${\rm Mo_2Ti_2C_3T_z}$ than in ${\rm Mo_2TiC_2T_z}$. It follows that the fraction of vacant sites in the Mo layers is higher in ${\rm Mo_2Ti_2C_3T_z}$, which may very well explain why the intrinsic mobility in the latter is only half the former. Recall that the DOS at ${\rm E_F}$ for MXenes in general and for the Mobased MXenes in particular is comprised mostly of Mo d-d orbitals, ³ and hence any defects in those layers would have a disproportionate effect on mobilities.

Lastly in this section, we find that mild (200 °C) annealing of the films in vacuum, which is thought to reduce internanosheet distances by removing water, and other intercalated species between the layers, almost doubles the intrinsic conductivity in a Mo₂Ti₂C₃T_z film but has a minimal effect on intrinsic THz conductivity in the Mo₂TiC₂T_z one. From XRD diffraction of the Mo₂Ti₂C₃T₂ films before and after annealing (Figure S3) we find that the d spacing decreases from 3.2 to 2.0 nm. This change is consistent with the increase in conductivity observed upon annealing. For reasons that are not clear the XRD patterns of the Mo₂Ti₂C₃T₂ films before and after annealing were more ambiguous (see Figure S3) and did not allow us to reach any conclusions concerning their interlayer spacings. However, given that in this case there was little change in conductivity, whatever changes that occurred in the *d* spacings, if any, did not alter the conductivity much.

3b. Time-Resolved THz Spectroscopy: Effect of Photoexcitation on Microscopic Conductivity. The transient photoconductivity dynamics after photoexcitation with 800 nm, 100 fs pulses are summarized in Figures 4 and 5 for the $Mo_2Ti_2C_3T_z$ and $Mo_2TiC_2T_z$ films, respectively. The first important observation is *the positive sign of the transient conductivity change* in both films, in stark contrast to our previous results for the metallic $Ti_3C_2T_z$, which exhibited a

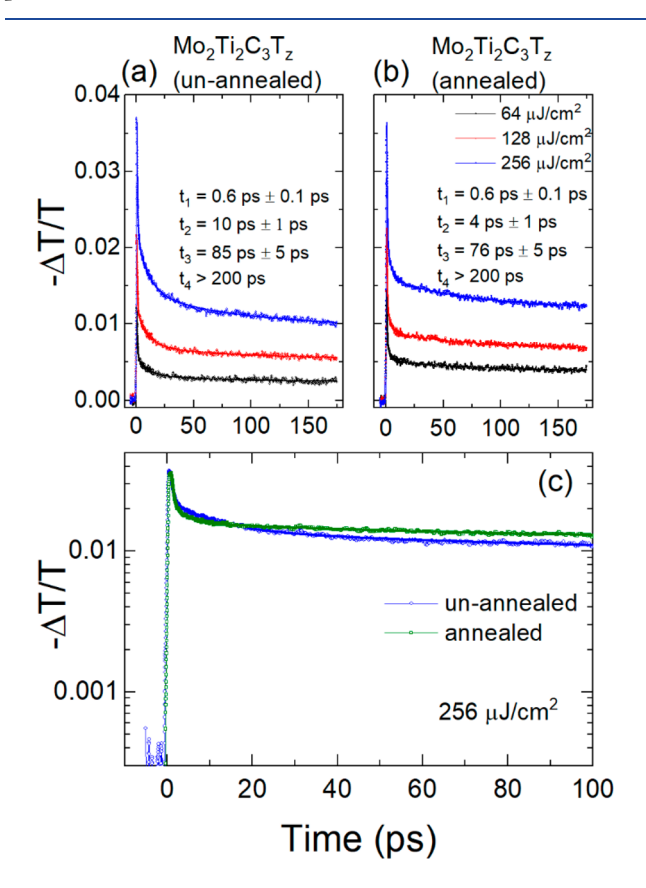


Figure 4. Transient photoconductivity, $(-\Delta T/T \propto \Delta \sigma)$, in $Mo_2Ti_2C_3T_z$ decays following excitation with 800 nm, 100 fs pulses with different fluence values, as indicated in the legend, for the (a) unannealed, as-deposited film and, (b) film annealed in vacuum at 200 °C. Same fluence values shown in (b) were used in (a). Experimental data are fitted to a multiexponential decay, and the resulting decay times, which are fluence-independent, are given in the panels. (c) Comparison of the transient photoconductivity decay for unannealed and annealed films.

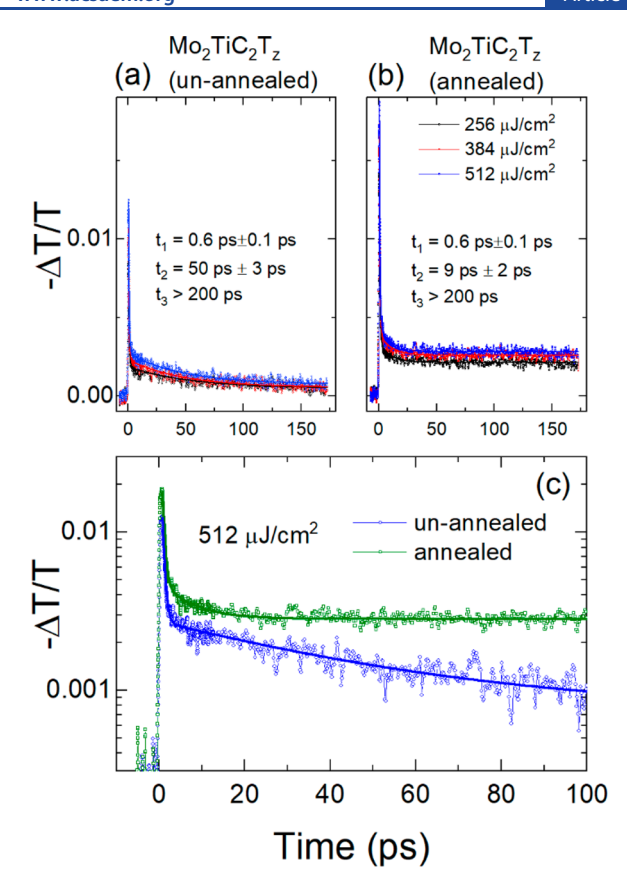


Figure 5. Transient photoconductivity, $(-\Delta T/T \propto \Delta \sigma)$, in $\text{Mo}_2\text{TiC}_2\text{T}_z$ decays following excitation with 800 nm, 100 fs pulses with different fluence values, as indicated in the legends, for the (a) unannealed, as-deposited film and (b) film annealed in vacuum at 200 °C. Same fluence values shown in (b) were used in (a). Experimental data are fitted to a multiexponential decay, and the resulting decay times are given in the graphs. (c) Comparison of the transient photoconductivity decay for unannealed and annealed films.

photoinduced suppression of conductivity. ¹⁵ Both $Mo_2Ti_2C_3T_z$ and $Mo_2TiC_2T_z$ are intrinsically metallic, albeit with a lower free carrier density. This transient increase in conductivity in response to optical excitation suggests that interband excitations inject a new population of free carriers (electrons and holes) into delocalized states above (or below, in the case of holes) E_F .

From these results the following observations are salient:

• Just like for the intrinsic conductivity, the observed photoconductivity peak immediately after optical excitation is higher in Mo₂Ti₂C₃T_z than in Mo₂TiC₂T_z. For example, at the same excitation fluence (256 μ J/ cm²), changes in the THz pulse peak transmissions for the Mo₂Ti₂C₃T₂ films are nearly three times stronger despite the thickness of this film being significantly smaller then in the $Mo_2TiC_3T_z$ case. In both films, the optical penetration depth at 800 nm is comparable to the film thickness (Figure S2), and most of the 800 nm pump is absorbed over the film's thickness. Therefore, lower observed peak photoconductivity in Mo₂TiC₂T_z suggests that a large fraction of photoinjected free carriers are trapped, or recombine, over time scales that are beyond the time resolution of our measurements, viz. <200 fs.

- In both films, peak photoconductivity immediately after excitation is followed by a multiexponential decay, presumably, as the photoinjected free carriers recombine, thermalize with the intrinsic carriers, and/or become trapped by defects.
- In both samples, at $t_1 \sim 0.6$ ps, the fastest decay component is quite fast. It becomes more pronounced with increased excitation fluence (and thus the number of optically injected free carriers density) and is unaffected by annealing. We therefore ascribe it to rapid, carrier density-dependent processes such as carrier—carrier scattering and, possibly, Auger recombination.
- In Mo₂Ti₂C₃T₂, we resolve three more decay slower components, one on the order of picoseconds and another on the order of tens of picoseconds, and a significantly slower one (>200 ps) that we cannot measure accurately as it extends well beyond our time range. The specific decay times are not affected by the excitation fluence in the studied range, and the contribution of the individual exponential components scales linearly with the fluence. In Mo₂TiC₂T₂, two more decay components are observed, in addition to the aforementioned 0.6 ps decay. One of them decays over tens of picoseconds, the other over >200 ps. It is reasonable to expect that similar carrier relaxation and trapping processes are present in both materials; in that is the case, then the relaxation process that we do not directly observe in Mo₂TiC₂T_z may occur over a much shorter time scale, beyond our experimental time resolution.
- Overall, when we compare the photoconductivity decays for the unannealed films, we find that the photoexcited excess free carriers remain delocalized for much longer in Mo₂Ti₂C₃T_z, with a photoconductivity at 100 ps after the excitation at nearly a third of its peak value. In the Mo₂TiC₂T_z film, that value is <10% which suggests a higher density of defect trap states that can efficiently capture photoexcited free carriers in this film.

Lastly in this section, we observe that annealing at 200 °C, which has previously been shown to remove water molecules and TBA⁺ ions trapped between the nanosheets in the film and decrease the internanosheet distance, ^{1,7} has only a minor effect on the magnitude of photoconductivity but leads to significant changes in the photoconductivity dynamics and free carrier lifetime. In both films, decay times of the processes that occur over picoseconds to tens of picoseconds shorten, while the slowest component (>200 ps) becomes more pronounced, as can be seen particularly clearly in the semilog plots in Figures 4c and 5c. The changes are much more dramatic in the case of Mo₂TiC₂T_z, however.

These results beg the questions: What processes are responsible for the observed photoconductivity dynamics, and why does the annealing have these effects? Before answering these questions, we can gain additional insight by analyzing the frequency-resolved, complex photoinduced conductivities at different times after optical excitation, within the Drude–Smith formalism. In TRTS, the unexcited sample serves as a reference. The photoconductivity spectra at a specific time after photoexcitation provide a snapshot of the

optically excited changes to the microscopic conductivity due to interband excitation of new carriers as well as the changes in mobility of existing carriers by intraband excitation and thermalization between the intrinsic and the photoinjected carriers. The photoconductivity spectra at three different times (5, 15, and 50 ps) after excitation for $Mo_2Ti_2C_3T_z$ films are shown in Figure 6. The results are shown before annealing (left

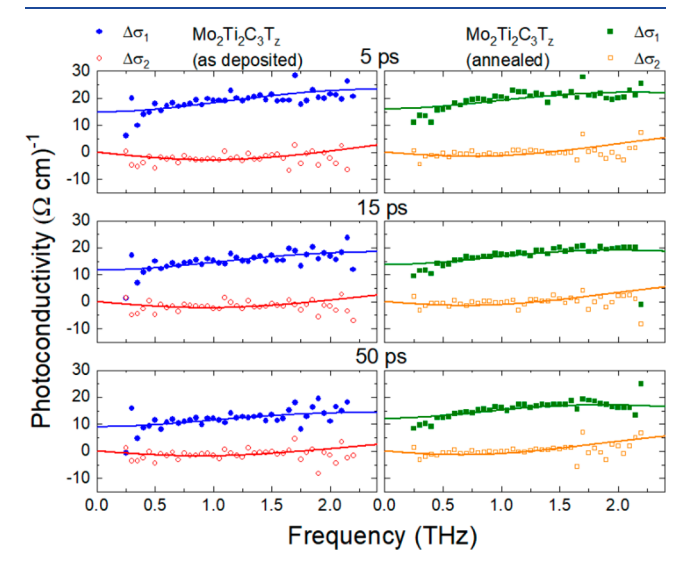


Figure 6. Photoinduced changes in complex THz conductivity in $Mo_2Ti_2C_3T_z$ at different times after excitation with $\sim\!256~\mu\mathrm{J/cm^2}$, 100 fs, 800 nm pulses for unannealed (left) and annealed (right) films. Solid and open symbols show real and imaginary conductivity components, respectively. Lines are fits of experimental data to the Drude–Smith model.

panels) and after (right panels in Figure 6). Figure 7 shows the photoconductivity spectra at three times (3, 5, and 20 ps) for the unannealed and annealed Mo₂TiC₂T₂ films.

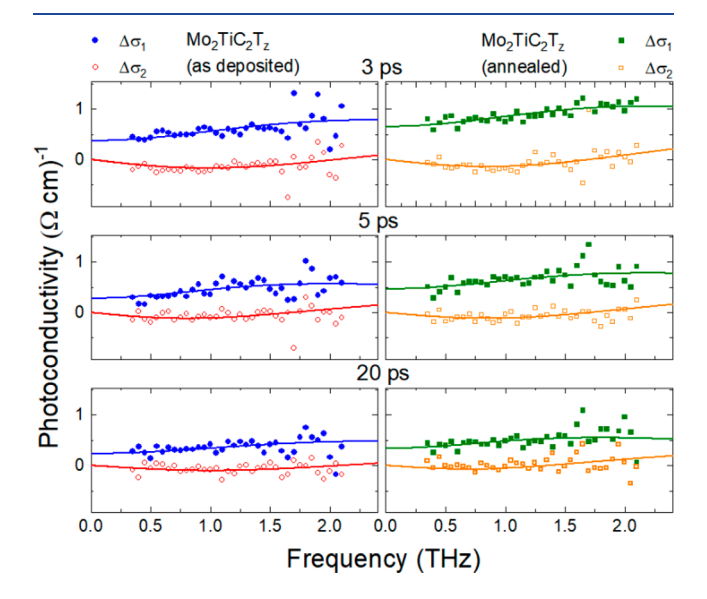


Figure 7. Photoinduced change in complex THz conductivity in $Mo_2TiC_2T_z$ at different times after excitation with $\sim 512~\mu J/cm^2$, 100 fs, 800 nm pulses for unannealed (left) and annealed (right) films. Solid and open symbols show real and imaginary conductivity components, respectively. Lines are fits of experimental data to Drude–Smith model.

For both MXenes, the shapes of the photoconductivity spectra are quite different from those of the intrinsic conductivity and exhibit less suppression of the real component at low frequencies. The scattering time and the c-parameters obtained by fitting the experimental data to the Drude-Smith model capture this difference. The 1.55 eV excitation creates a population of free carriers (electrons and holes) that have longer scattering times compared to the intrinsic free carriers and experience a less negative *c*-parameter (-0.67 vs -0.94 for the unannealed Mo₂Ti₂C₃T_z film and -0.75 vs -0.86 for $Mo_2TiC_2T_z$ film - see Table 1),

Table 1. Drude-Smith c-Parameter for Intrinsic and Photoexcited Carriers in Unannealed and Annealed Mo₂Ti₂C₃T_z and Mo₂TiC₂T_z Films

	$\mathrm{Mo_2Ti_2C_3T}_z$	${\rm Mo_2TiC_2T}_z$
intrinsic carriers, unannealed	-0.941 ± 0.007	-0.864 ± 0.013
intrinsic carriers, annealed	-0.875 ± 0.013	-0.895 ± 0.005
photoexcited carriers, unannealed	-0.67 ± 0.02	-0.75 ± 0.02
photoexcited carriers, annealed	-0.62 ± 0.02	-0.69 ± 0.02

demonstrating the higher long-range, internanosheet mobility compared to the intrinsic free carriers (Table 1). This suggests that an optical pulse injects a population of electrons (holes) into delocalized bands at the energies above (below) the Fermi level, E_F. We find that these extrinsic carriers are less affected by the internanosheet boundaries compared to the intrinsic carriers at E_E.

Over the time scales given by the photoconductivity dynamics (Figures 4 and 5), those excess carriers become trapped by the available defect states, recombine, and eventually relax back to the ground state.

Looking more closely at the Mo₂Ti₂C₃T₂ film results, the magnitude of the photoinduced conductivity—at 5 ps in the DC limit after photoexcitation with a 256 μ I/cm² pulse—is nearly one-third of the magnitude of the intrinsic conductivity and changes little up to 50 ps after photoexcitation. At the same time, the excess carrier density, estimated from the Drude-Smith fitting with m^* approximated by m_e , is only \sim 1% of the intrinsic carrier density at \sim 10¹⁸ cm⁻³. This observation underscores that optically injected carriers have higher short-range, intrananosheet, as well as long-range, internanosheet, mobility and therefore contribute significantly more to conductivity. Annealing causes subtle changes in the spectral shape. Fitting the data to the Drude-Smith model, we find that annealing results in a small but detectable increase in the c-parameter experienced by the photoexcited carriers from -0.67 ± 0.02 to -0.62 ± 0.02 . This implies that, like for the intrinsic carriers, annealing enhances intrananosheet transport for photoexcited carriers. This presumably results from the reduced intrananosheet spacing as confirmed by XRD diffraction. The scattering time (and therefore the average photoexcited carrier mobility) varies between ~75 fs to ~50 fs with time and excitation (Figure 8).

Figure 8 plots the scattering time, τ_{DS} , as a function of photoexcited carrier density scaled by the effective mass extracted from the Drude-Smith fitting of data at different times and excitation fluences. Here the scattering time increases at lower carrier densities, a hallmark that carriercarrier scattering plays a prominent role at high carrier densities. 45,46 Annealing increases carrier scattering time in Mo₂Ti₂C₃T_z, an increase we hypothesize results from the

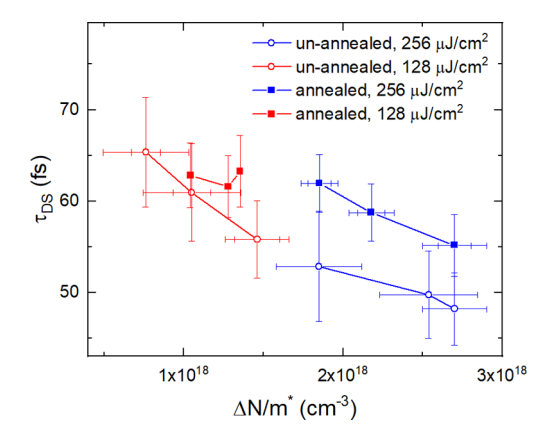


Figure 8. Scattering time τ as a function of photoexcited carrier density in Mo₂Ti₂C₃T_z scaled by the effective mass, extracted by fitting the complex photoconductivity spectra at different times after excitation and different excitation fluence values for unannealed (open symbols) and annealed (solid symbols) samples.

removal of intercalated species present on the surfaces of the nanosheets, which affect the motion of carries in the conductive core regions of the nanosheets by causing potential fluctuations. The combined effect of improved intrananosheet and internanosheet carrier mobility, represented by the changes in both scattering time τ_{DC} and the c-parameter, is probably responsible for the improved carrier transport in annealed Mo₂Ti₂C₃T_z. These observed, annealing-induced changes in mobility of free carriers and their ability to move between neighboring nanosheets may help explain changes in dynamics. If the intermediate time-scale photoconductivity decay components, ~10 ps and ~85 ps (~4 and 76 ps after annealing), represent trapping of mobile carriers by defects near nanosheet edges, then the higher mobility and improved internanosheet transport in the annealed film facilitates it. Said otherwise, the better long-range mobility results in faster trapping of the photoinduced carriers at nanosheet boundaries. Carrier trapping and recombination at point defects within the individual nanosheets is likely responsible for the slowest, >200 ps, decay component which is slowed after annealing, suggesting that mild annealing may "heal" some of the point defects. Alternatively, annealing may lessen their deleterious effect by removing water and other intercalants from their vicinity if those species are co-located with the point defects that facilitate carrier trapping.

The photoinduced conductivity in the Mo₂TiC₂T_z films (Figure 7) is an order of magnitude smaller than in the Mo₂Ti₂C₃T_z films, even at early times as presumably most photoexcited carriers recombine or become localized over very short time scales. For a small fraction of photoexcited delocalized carriers that remain after the initial fast decay, the photoconductivity spectra share many similarities with Mo₂Ti₂C₃T_z. Again, carrier scattering time (and therefore the intrananosheet mobility) is higher than that for the intrinsic free carriers (60 \pm 5 fs vs 36 \pm 4 fs). This scattering time is unchanged for different times after excitation and excitation fluence values, as the low photoinjected carrier density does not allow for a significant carrier-carrier scattering contribution. Moreover, unlike the Mo₂Ti₂C₃T_z film, annealing does not significantly impact the carrier scattering time in Mo₂TiC₂T_z. It does, however, improve internanosheet transport, as evidenced by changes in the c-parameter from $-0.75 \pm$ 0.02 to -0.69 ± 0.02 after annealing. Again, this c-parameter is less negative than the one characterizing the intrinsic, not photoexcited, carriers, suggesting that photoexcitation generated a new population of delocalized carriers that have an easier time traveling between nanosheets. Looking back at the photoconductivity dynamics (Figure 5), annealing has a much more dramatic effect on the lifetime of photoexcited carriers in Mo₂TiC₂T_z than Mo₂Ti₂C₃T_z, which may imply a larger density of both defects at the nanosheet edges and point defects within the nanosheets. Presumed edge trapping time reduces considerably in the annealed film, from ~50 ps to ~9 ps, as internanosheet hopping is enhanced, as evidenced by the change in the *c*-parameter. The longer time scale component is also dramatically slowed, as can be best seen in Figure 5c, suggesting that Mo₂TiC₂T₂ nanosheets are more susceptible to the deleterious effects of point defects and intercalated species on the lifetime of photoinduced carriers.

A recent XPS study on $Mo_2TiC_2T_z$ and $Mo_2Ti_2C_3T_z$ films concluded that the harsh conditions needed to etch these phases into monolayers result in their partial oxidation.⁴⁴ The TBAOH used to delaminate the monolayers resulted in further oxidation and a reduction in the F-content. In all cases, etching resulted in a decrease in the Ti to Mo ratio and the loss of Ti also resulted in the loss of C atoms. The Ti atoms lost are presumed to be ones that had substituted for Mo in the outer layers. 47 Evidence was also presented for O substituting for Cvacancies. It follows that in the final analysis the microstructures of the films fabricated is quite complicated, which partially explains the complex transport response observed herein. Needless to say, much more work, beyond the scope of this paper, is needed to fully understand the subtle interactions between electronic transport, defects in general, and point defects in particular. This comment notwithstanding, the results obtained herein are an excellent first attempt at fleshing out some of these interactions. There are few other techniques that can do that.

4. SUMMARY AND CONCLUSIONS

An overall better picture of the microscopic carrier mobility and carrier dynamics in Mo-containing MXenes emerges from the results shown herein and earlier temperature-dependent transport measurements. Demonstrated previously to be metallic, individual 2D Mo₂Ti₂C₃T_z and Mo₂TiC₂T_z nanosheets have high intrinsic carrier densities (on the order of 10²⁰ cm⁻³). These intrinsic free carriers, as well as excess carriers injected by intraband optical excitations, experience band-like, delocalized transport within individual nanosheets.

However, the internanosheet boundaries strongly suppress long-range transport in these films. The long-range, internanosheet mobilities of the intrinsic carriers are nearly an order of magnitude lower than their short-range, intrananosheet mobilities. Our results are consistent with those of Halim et al., who concluded that VRH, with possibly a contribution of thermally activated transport at temperatures > 130 K, is the operative mechanism for carriers to move between the individual 2D nanosheets. 1

In stark contrast to $Ti_3C_2T_z$ films where we have recently reported suppression of conductivity by optical excitation, here we find that optical excitation with 1.55 eV photons increases conductivity of both $Mo_2Ti_2C_3T_z$ and $Mo_2TiC_2T_z$ films. This enhancement is presumed to occur by injecting additional free carriers by intraband optical excitations. Both short-range (intrananosheet) and long-range (internanosheet) mobilities are higher for the photoexcited carriers compared to the

intrinsic carriers, most probably because they reside in higher energy states with different average band curvatures.

Annealing further improves short- and long-range carrier transport of photoexcited carriers in both studied films. We conjecture that trapping at point defects within the nanosheets and/or at the nanosheet edges and interfaces rapidly reduces the photoexcited carrier density within the first tens of picoseconds, and that these processes are even faster after annealing when internanosheet transport is improved. However, a fraction of the photoexcited carriers survives for substantially longer periods, well over 200 ps, suggesting that these carriers are confined within the nanosheets. This fraction is significantly higher in $\text{Mo}_2\text{Ti}_2\text{C}_3\text{T}_z$ than in $\text{Mo}_2\text{Ti}\text{C}_2\text{T}_z$; in both cases, it is increased after annealing.

In summary, Mo-based MXenes exhibit optical absorption across the visible and near-infrared range. Unlike ${\rm Ti}_3{\rm C}_2{\rm T}_z$, where photoexcitation suppresses conductivity, the Mo-based MXenes demonstrate a higher and longer-lived photoinduced conductivity. These observations highlight a wide range of properties that can be achieved by engineering MXene's structure and composition. In the specific cases of ${\rm Mo}_2{\rm Ti}_2{\rm C}_3{\rm T}_z$ and ${\rm Mo}_2{\rm Ti}_{\rm C}_2{\rm T}_z$, their properties render them attractive for a whole host of optoelectronic, sensing, and photoelectrochemical applications.

ASSOCIATED CONTENT

5 Supporting Information

The Supporting Information is available free of charge at https://pubs.acs.org/doi/10.1021/acsaem.9b01966.

Representative SEM images, UV—vis spectroscopy of MXene films, and XRD diffraction patterns of Mo-based films (PDF)

AUTHOR INFORMATION

Corresponding Author

Lyubov V. Titova — Department of Physics, Worcester Polytechnic Institute, Worcester, Massachusetts 01609, United States; orcid.org/0000-0002-2146-9102; Email: ltitova@ wpi.edu

Authors

Guangjiang Li – Department of Physics, Worcester Polytechnic Institute, Worcester, Massachusetts 01609, United States

Varun Natu — Department of Materials Science and Engineering, Drexel University, Philadelphia, Pennsylvania 19104, United States

Teng Shi — Department of Physics, Worcester Polytechnic Institute, Worcester, Massachusetts 01609, United States Michel W. Barsoum — Department of Materials Science and

Engineering, Drexel University, Philadelphia, Pennsylvania 19104, United States; oorcid.org/0000-0001-7800-3517

Complete contact information is available at: https://pubs.acs.org/10.1021/acsaem.9b01966

Author Contributions

§These authors contributed equally.

Notes

The authors declare no competing financial interest.

ACKNOWLEDGMENTS

We thank Dr. Thierry Ouisse for insightful discussions, Maryam Masroor Shalmani for assistance with the annealing of samples, and Binod Giri for assistance with SEM imaging. This work was funded by NSF (DMR 1740795).

REFERENCES

- (1) Halim, J.; Moon, E. J.; Eklund, P.; Rosen, J.; Barsoum, M. W.; Ouisse, T. Variable range hopping and thermally activated transport in molybdenum-based MXenes. *Phys. Rev. B: Condens. Matter Mater. Phys.* **2018**, *98* (10), 104202.
- (2) Halim, J.; Kota, S.; Lukatskaya, M. R.; Naguib, M.; Zhao, M.-Q.; Moon, E. J.; Pitock, J.; Nanda, J.; May, S. J.; Gogotsi, Y.; Barsoum, M. W. Synthesis and Characterization of 2D Molybdenum Carbide (MXene). *Adv. Funct. Mater.* **2016**, *26* (18), 3118–3127.
- (3) Anasori, B.; Shi, C.; Moon, E. J.; Xie, Y.; Voigt, C. A.; Kent, P. R. C.; May, S. J.; Billinge, S. J. L.; Barsoum, M. W.; Gogotsi, Y. Control of electronic properties of 2D carbides (MXenes) by manipulating their transition metal layers. *Nanoscale Horizons* **2016**, *I* (3), 227–234.
- (4) Khazaei, M.; Ranjbar, A.; Arai, M.; Yunoki, S. Topological insulators in the ordered double transition metals M₂·M"C₂ MXenes (M'=Mo, W; M"=Ti, Zr, Hf). *Phys. Rev. B: Condens. Matter Mater. Phys.* **2016**, 94 (12), 125152.
- (5) Halim, J.; Persson, I.; Moon, E. J.; Kühne, P.; Darakchieva, V.; Persson, P. O. Å.; Eklund, P.; Rosen, J.; Barsoum, M. W. Electronic and optical characterization of 2D Ti2C and Nb2C (MXene) thin films. J. Phys.: Condens. Matter 2019, 31 (16), 165301.
- (6) Khazaei, M.; Ranjbar, A.; Arai, M.; Sasaki, T.; Yunoki, S. Electronic properties and applications of MXenes: a theoretical review. *J. Mater. Chem. C* **2017**, *5* (10), 2488–2503.
- (7) Hart, J. L.; Hantanasirisakul, K.; Lang, A. C.; Anasori, B.; Pinto, D.; Pivak, Y.; van Omme, J. T.; May, S. J.; Gogotsi, Y.; Taheri, M. L. Control of MXenes' electronic properties through termination and intercalation. *Nat. Commun.* **2019**, *10* (1), 522.
- (8) Dillon, A. D.; Ghidiu, M. J.; Krick, A. L.; Griggs, J.; May, S. J.; Gogotsi, Y.; Barsoum, M. W.; Fafarman, A. T. Highly Conductive Optical Quality Solution-Processed Films of 2D Titanium Carbide. *Adv. Funct. Mater.* **2016**, 26 (23), 4162–4168.
- (9) Ghidiu, M.; Lukatskaya, M. R.; Zhao, M.-Q.; Gogotsi, Y.; Barsoum, M. W. Conductive two-dimensional titanium carbide 'clay' with high volumetric capacitance. *Nature* **2014**, *516*, 78.
- (10) Ali, A.; Belaidi, A.; Ali, S.; Helal, M. I.; Mahmoud, K. A. Transparent and conductive Ti3C2Tx (MXene) thin film fabrication by electrohydrodynamic atomization technique. *J. Mater. Sci.: Mater. Electron.* **2016**, 27 (5), 5440–5445.
- (11) Dong, Y.; Chertopalov, S.; Maleski, K.; Anasori, B.; Hu, L.; Bhattacharya, S.; Rao, A. M.; Gogotsi, Y.; Mochalin, V. N.; Podila, R. Saturable Absorption in 2D ${\rm Ti}_3{\rm C}_2$ MXene Thin Films for Passive Photonic Diodes. *Adv. Mater.* **2018**, *30* (10), 1705714.
- (12) Han, M.; Yin, X.; Wu, H.; Hou, Z.; Song, C.; Li, X.; Zhang, L.; Cheng, L. Ti3C2MXenes with Modified Surface for High-Performance Electromagnetic Absorption and Shielding in the X-Band. ACS Appl. Mater. Interfaces 2016, 8 (32), 21011–21019.
- (13) Jhon, Y. I.; Koo, J.; Anasori, B.; Seo, M.; Lee, J. H.; Gogotsi, Y.; Jhon, Y. M. Metallic MXene Saturable Absorber for Femtosecond Mode-Locked Lasers. *Adv. Mater.* **2017**, *29* (40), 1702496.
- (14) Jiang, X.; Liu, S.; Liang, W.; Luo, S.; He, Z.; Ge, Y.; Wang, H.; Cao, R.; Zhang, F.; Wen, Q.; Li, J.; Bao, Q.; Fan, D.; Zhang, H. Broadband Nonlinear Photonics in Few-Layer MXene $Ti_3C_2T_x$ (T = F, O, or OH). Laser & Photonics Reviews 2018, 12 (2), 1700229.
- (15) Li, G.; Kushnir, K.; Dong, Y.; Chertopalov, S.; Rao, A. M.; Mochalin, V. N.; Podila, R.; Titova, L. V. Equilibrium and non-equilibrium free carrier dynamics in 2D Ti 3 C 2 T x MXenes: THz spectroscopy study. 2D Mater. 2018, 5 (3), 035043.
- (16) Zhang, C.; Anasori, B.; Seral-Ascaso, A.; Park, S. H.; McEvoy, N.; Shmeliov, A.; Duesberg, G. S.; Coleman, J. N.; Gogotsi, Y.; Nicolosi, V. Transparent, Flexible, and Conductive 2D Titanium Carbide (MXene) Films with High Volumetric Capacitance. *Adv. Mater.* **2017**, 29 (36), 1702678.
- (17) Shahzad, F.; Alhabeb, M.; Hatter, C. B.; Anasori, B.; Man Hong, S.; Koo, C. M.; Gogotsi, Y. Electromagnetic interference

- shielding with 2D transition metal carbides (MXenes). *Science* **2016**, 353 (6304), 1137–1140.
- (18) Miranda, A.; Halim, J.; Barsoum, M. W.; Lorke, A. Electronic properties of freestanding $\text{Ti}_3\text{C}_2\text{T}_x$ MXene monolayers. *Appl. Phys. Lett.* **2016**, *108* (3), 033102.
- (19) Anasori, B.; Xie, Y.; Beidaghi, M.; Lu, J.; Hosler, B. C.; Hultman, L.; Kent, P. R. C.; Gogotsi, Y.; Barsoum, M. W. Two-Dimensional, Ordered, Double Transition Metals Carbides (MXenes). ACS Nano 2015, 9 (10), 9507–9516.
- (20) Jepsen, P. U.; Cooke, D. G.; Koch, M. Terahertz spectroscopy and imaging—Modern techniques and applications. *Laser & Photonics Reviews* **2011**, *5* (1), 124–166.
- (21) Baxter, J. B.; Guglietta, G. W. Terahertz spectroscopy. *Anal. Chem.* **2011**, *83* (12), 4342–68.
- (22) Cunningham, P. D.; McCreary, K. M.; Hanbicki, A. T.; Currie, M.; Jonker, B. T.; Hayden, L. M. Charge Trapping and Exciton Dynamics in Large-Area CVD Grown MoS2. *J. Phys. Chem. C* **2016**, 120 (10), 5819–5826.
- (23) Cunningham, P. D.; Hayden, L. M.; Yip, H. L.; Jen, A. K. Y. Charge Carrier Dynamics in Metalated Polymers Investigated by Optical-Pump Terahertz-Probe Spectroscopy. *J. Phys. Chem. B* **2009**, 113 (47), 15427–15432.
- (24) Laforge, J. M.; Cocker, T. L.; Beaudry, A. L.; Cui, K.; Tucker, R. T.; Taschuk, M. T.; Hegmann, F. A.; Brett, M. J. Conductivity control of as-grown branched indium tin oxide nanowire networks. *Nanotechnology* **2014**, *25* (3), 035701.
- (25) Ülbricht, R.; Hendry, E.; Shan, J.; Heinz, T. F.; Bonn, M. Carrier dynamics in semiconductors studied with time-resolved terahertz spectroscopy. *Rev. Mod. Phys.* **2011**, *83* (2), 543–586.
- (26) Butler, K. T.; Dringoli, B. J.; Zhou, L.; Rao, P. M.; Walsh, A.; Titova, L. V. Ultrafast carrier dynamics in BiVO₄ thin film photoanode material: interplay between free carriers, trapped carriers and low-frequency lattice vibrations. *J. Mater. Chem. A* **2016**, *4* (47), 18516–18523.
- (27) Titova, L. V.; Cocker, T. L.; Xu, S.; Baribeau, J.-M.; Wu, X.; Lockwood, D. J.; Hegmann, F. A. Ultrafast carrier dynamics and the role of grain boundaries in polycrystalline silicon thin films grown by molecular beam epitaxy. *Semicond. Sci. Technol.* **2016**, 31 (10), 105017.
- (28) Lloyd-Hughes, J.; Jeon, T.-I. A Review of the Terahertz Conductivity of Bulk and Nano-Materials. *J. Infrared, Millimeter, Terahertz Waves* **2012**, 33 (9), 871–925.
- (29) Beard, M. C.; Turner, G. M.; Schmuttenmaer, C. A. Transient photoconductivity in GaAs as measured by time-resolved terahertz spectroscopy. *Phys. Rev. B: Condens. Matter Mater. Phys.* **2000**, 62 (23), 15764–15777.
- (30) Demsar, J.; Dekorsy, T. Carrier dynamics in bulk semi-conductors and metals after ultrashort pulse excitation. *Opt. Tech. Solid-State Mater. Charact.* **2016**, 291–328.
- (31) Ouisse, T.; Barsoum, M. W. Magnetotransport in the MAX phases and their 2D derivatives: MXenes. *Mater. Res. Lett.* **2017**, 5 (6), 365–378.
- (32) Xin, X.; Altan, H.; Saint, A.; Matten, D.; Alfano, R. R. Terahertz absorption spectrum of para and ortho water vapors at different humidities at room temperature. *J. Appl. Phys.* **2006**, *100* (9), 094905.
- (33) Cocker, T. L.; Titova, L. V.; Fourmaux, S.; Bandulet, H. C.; Brassard, D.; Kieffer, J. C.; El Khakani, M. A.; Hegmann, F. A. Terahertz conductivity of the metal-insulator transition in a nanogranular VO₂ film. *Appl. Phys. Lett.* **2010**, *97* (22), 221905.
- (34) Cocker, T. L.; Baillie, D.; Buruma, M.; Titova, L. V.; Sydora, R. D.; Marsiglio, F.; Hegmann, F. A. Microscopic origin of the Drude-Smith model. *Phys. Rev. B: Condens. Matter Mater. Phys.* **2017**, *96* (20), 205439.
- (35) Jensen, S. A.; Ulbricht, R.; Narita, A.; Feng, X.; Mullen, K.; Hertel, T.; Turchinovich, D.; Bonn, M. Ultrafast photoconductivity of graphene nanoribbons and carbon nanotubes. *Nano Lett.* **2013**, *13* (12), 5925–30.
- (36) Guglietta, G. W.; Diroll, B. T.; Gaulding, E. A.; Fordham, J. L.; Li, S.; Murray, C. B.; Baxter, J. B. Lifetime, Mobility, and Diffusion of

- Photoexcited Carriers in Ligand-Exchanged Lead Selenide Nanocrystal Films Measured by Time-Resolved Terahertz Spectroscopy. *ACS Nano* **2015**, *9* (2), 1820–1828.
- (37) Richter, C.; Schmuttenmaer, C. A. Exciton-like trap states limit electron mobility in TiO₂ nanotubes. *Nat. Nanotechnol.* **2010**, *5*, 769.
- (38) Alberding, B. G.; DeSario, P. A.; So, C. R.; Dunkelberger, A. D.; Rolison, D. R.; Owrutsky, J. C.; Heilweil, E. J. Static and Time-Resolved Terahertz Measurements of Photoconductivity in Solution-Deposited Ruthenium Dioxide Nanofilms. *J. Phys. Chem. C* **2017**, *121* (7), 4037–4044.
- (39) Alberding, B. G.; Kushto, G. P.; Lane, P. A.; Heilweil, E. J. Reduced photoconductivity observed by time-resolved terahertz spectroscopy in metal nanofilms with and without adhesion layers. *Appl. Phys. Lett.* **2016**, *108* (22), 223104.
- (40) Walther, M.; Cooke, D. G.; Sherstan, C.; Hajar, M.; Freeman, M. R.; Hegmann, F. A. Terahertz conductivity of thin gold films at the metal-insulator percolation transition. *Phys. Rev. B: Condens. Matter Mater. Phys.* **2007**, 76 (12), 125408.
- (41) Titova, L. V.; Cocker, T. L.; Cooke, D. G.; Wang, X.; Meldrum, A.; Hegmann, F. A. Ultrafast percolative transport dynamics in silicon nanocrystal films. *Phys. Rev. B: Condens. Matter Mater. Phys.* **2011**, 83 (8), 085403.
- (42) Baxter, J. B.; Schmuttenmaer, C. A. Conductivity of ZnO nanowires, nanoparticles, and thin films using time-resolved terahertz spectroscopy. *J. Phys. Chem. B* **2006**, *110* (50), 25229–25239.
- (43) Cooke, D. G.; Meldrum, A.; Uhd Jepsen, P. Ultrabroadband terahertz conductivity of Si nanocrystal films. *Appl. Phys. Lett.* **2012**, *101* (21), 211107.
- (44) Halim, J.; Cook, K. M.; Eklund, P.; Rosen, J.; Barsoum, M. W. XPS of cold pressed multilayered and freestanding delaminated 2D thin films of Mo2TiC2Tz and Mo2Ti2C3Tz (MXenes). *Appl. Surf. Sci.* **2019**, *494*, 1138–1147.
- (45) Mics, Z.; D'Angio, A.; Jensen, S. A.; Bonn, M.; Turchinovich, D. Density-dependent electron scattering in photoexcited GaAs in strongly diffusive regime. *Appl. Phys. Lett.* **2013**, *102* (23), 231120.
- (46) Sharma, G.; Al-Naib, I.; Hafez, H.; Morandotti, R.; Cooke, D. G.; Ozaki, T. Carrier density dependence of the nonlinear absorption of intense THz radiation in GaAs. *Opt. Express* **2012**, 20 (16), 18016–18024.
- (47) Anasori, B.; Dahlqvist, M.; Halim, J.; Moon, E. J.; Lu, J.; Hosler, B. C.; Caspi, E. a. N.; May, S. J.; Hultman, L.; Eklund, P.; Rosén, J.; Barsoum, M. W. Experimental and theoretical characterization of ordered MAX phases Mo2TiAlC2 and Mo2Ti2AlC3. *J. Appl. Phys.* **2015**, *118* (9), 094304.